Critical properties and charge transport in ethylene bridged organosilica low-κ dielectrics

Timofey V. Perevalov (iD), Andrei A. Gismatulin, Dmitry S. Seregin (iD), Yingjie Wang, Haoyu Xu, Vladimir N. Kruchinin, Evgeniy V. Spesivcev, Vladimir A. Gritsenko, Kamil' A. Nasyrov, Igor' P. Prosvirin (iD), Jing Zhang (iD), Konstantin A. Vorotilov (iD), and Mikhail R. Baklanov (iD)

View Online   Export Citation   CrossMark

127, 195105

Critical properties and charge transport in ethylene bridged organosilica low-κ dielectrics

Timofey V. Perevalov,[1,2,a] Andrei A. Gismatulin,[1] Dmitry S. Seregin,[3] Yingjie Wang,[4] Haoyu Xu,[4]
Vladimir N. Kruchinin,[1] Evgeniy V. Spesivcev,[1] Vladimir A. Gritsenko,[1,2,5] Kamil' A. Nasyrov,[6] Igor' P. Prosvirin,[7]
Jing Zhang,[4] Konstantin A. Vorotilov,[3] and Mikhail R. Baklanov[3,4]

AFFILIATIONS

[1]Rzhanov Institute of Semiconductor Physics SB RAS, 13 Lavrentiev Ave., 630090 Novosibirsk, Russia
[2]Novosibirsk State University, 2 Pirogov Str., 630090 Novosibirsk, Russia
[3]MIREA, Russian Technological University, 78 Vernadsky Ave., 119454 Moscow, Russia
[4]North China University of Technology, 5 Jinyuanzhuang Rd., Shijingshan District, Beijing 100144, China
[5]Novosibirsk State Technical University, 20 Marks Ave., 630073 Novosibirsk, Russia
[6]Institute of Automation and Electrometry, 1 Koptyug Ave., 630090 Novosibirsk, Russia
[7]Boreskov Institute of Catalysis, SB RAS, 5 Lavrentiev Ave., 630090 Novosibirsk, Russia

[a]Author to whom correspondence should be addressed: timson@isp.nsc.ru

ABSTRACT

Organosilicate-glass-based low-κ films containing both terminal methyl groups and an ethylene bridge between the silicon atoms are spin-on deposited by using 1,2-bis(trimethoxysilyl)ethane and methyltrimethoxysilane, Brij30 template, and thermal curing. The chemical composition, porosity, and internal defects are studied using Fourier-transform infrared spectroscopy, x-ray photoelectron spectroscopy, electron energy loss spectroscopy, UV induced luminescence, and ellipsometric porosimetry. It was found that the studied films contain oxygen-deficient centers (Si—Si bonds). The high defect density of the states near the valence-band edge of the studied low-κ films leads to a relatively small bandgap value of about 6.3 eV. The current–voltage characteristics at different temperatures were analyzed using six theoretical charge transport models where the transport is limited by the traps ionization. It was found that the best qualitative and quantitative agreement between the calculations and experimental data is achieved by using the model of phonon-assisted electron tunneling between the neutral traps and is supplemented by considering the space charge and charge carrier kinetics. Since the thermal and optical energies of the traps in the studied films are 1.6 eV and 3.2 eV, respectively, it is concluded that the traps are responsible for the charge transport in the Si—Si bonds.

Published under license by AIP Publishing. https://doi.org/10.1063/1.5145239

I. INTRODUCTION

Advanced interconnects of ULSI (Ultra Large Scale Integration) devices require low resistivity conducting wires isolated by low dielectric constant materials to reduce the signal propagation delay (resistive–capacitive or RC delay), dynamic power consumption, and crosstalk noise.[1,2] For this reason, the traditional Al conductor was replaced by Cu about 25 years ago when the semiconductor industry started implementation of a 90 nm technology node. Different alternative metals (Mo, W, Co, Ru, etc.) and non-metallic conductors (carbon nanotubes, graphene) have also been evaluated during the last two decades. At the same time, extensive search and exploration

of dielectric materials with low dielectric permittivity (low-κ dielectrics) were carried out.[3–7] Finally, organosilicate glass (OSG) materials were selected as the most suitable for the existing microelectronics technology. They can be deposited by using the spin-on deposition [the sol-gel method and the chemical solution deposition (CSD) method] or plasma enhanced chemical vapor deposition (PECVD) method. PECVD is currently the preferred method in the microelectronics industry because it can be easily integrated into the existing device manufacturing processes. However, it was found that PECVD meets serious challenges when it is necessary to deposit the films with the ultralow κ value smaller than 2.5.[7,8] For this reason, spin-on

deposited low-κ films are a subject of increasing interest. They not only allow easy scaling of the dielectric constant below 2.5, but are also more suitable for an alternative (subtractive) integration scheme when the metal is patterned first and then the gaps are filled by the spin-on deposited OSG material.[7,9,10]

The next generation of interlayer dielectric materials needs to be carefully selected to reduce the κ value, while still providing the required mechanical and chemical stability necessary for their integration and packaging. It has been proven that a significant improvement of the mechanical properties of low-κ films can be achieved by incorporating the carbon bridges between Si atoms instead of oxygen atoms.[7,11,12] A comparative analysis of OSG materials with terminal methyl groups and with the ethylene bridge between the Si atoms has recently been reported.[10] It was shown that the films with the ethylene bridge has a larger Young's modulus that makes them more attractive for practical applications.

In the present work, porous spin-on deposited low-κ films containing ethylene bridging groups are studied. The Si-CH$_2$-CH$_2$-Si (ethylene) bridging groups are uniformly distributed into the pore's walls, and the pores are ordered so that they form Periodic Mesoporous Organosilicas (PMOs) (Fig. 1). The terminal methyl groups are also present on the pore surface defining the low-κ film's hydrophobicity, which is a necessary condition for avoiding the moisture adsorption.

To improve the performance and reliability of IC interconnects based on Cu and low-κ dielectrics, it is important to understand the leakage current nature in low-κ films. In turn, this implies the establishment of a charge transport mechanism and the identification of the defects responsible for the leakage current. It is important to understand the defects' nature in low-κ dielectrics to meet the requirements of electronic devices and to optimize the low-κ synthesis. Thus, the charge transport mechanism and the trap nature of low-κ films are a matter that requires a detailed investigation.

A significant number of publications have already been devoted to the study of electrical properties and the reliability of PECVD low-κ dielectrics with terminal methyl groups. These studies are mainly related to the mechanisms of an electrical breakdown and also include an analysis of the most important factors affecting the leakage current. One can mention the excellent review written by Ogawa and Aubel and the corresponding references.[13] It has been shown that the electrical properties of low-κ dielectrics are highly affected by the integration procedure including plasma damage after patterning[14] and barrier deposition,[15,16] the interface of low-κ dielectrics with metal barriers,[13] and the presence of sp^2 carbons as porogen residues.[17]

Three conduction mechanisms have been reported for the methyl terminated low-κ dielectrics.[18] The Schottky emission (SE) and the Poole–Frenkel (PF) emission describe a field-enhanced thermal excitation of electrons entering the conduction band from the low-κ interface and the trap states with coulomb potentials, respectively. Fowler–Nordheim (FN) tunneling conduction is caused by electrons tunneling from the metal Fermi energy or trapping sites in the material itself into the low-κ dielectric conduction band. Particularly, it was shown that the leakage currents in the PECVD OSG (SiCOH) dielectric can be described by the Frenkel mechanism and by the space charge limited current model.[19] This conclusion was based on the simulation of current–voltage characteristics
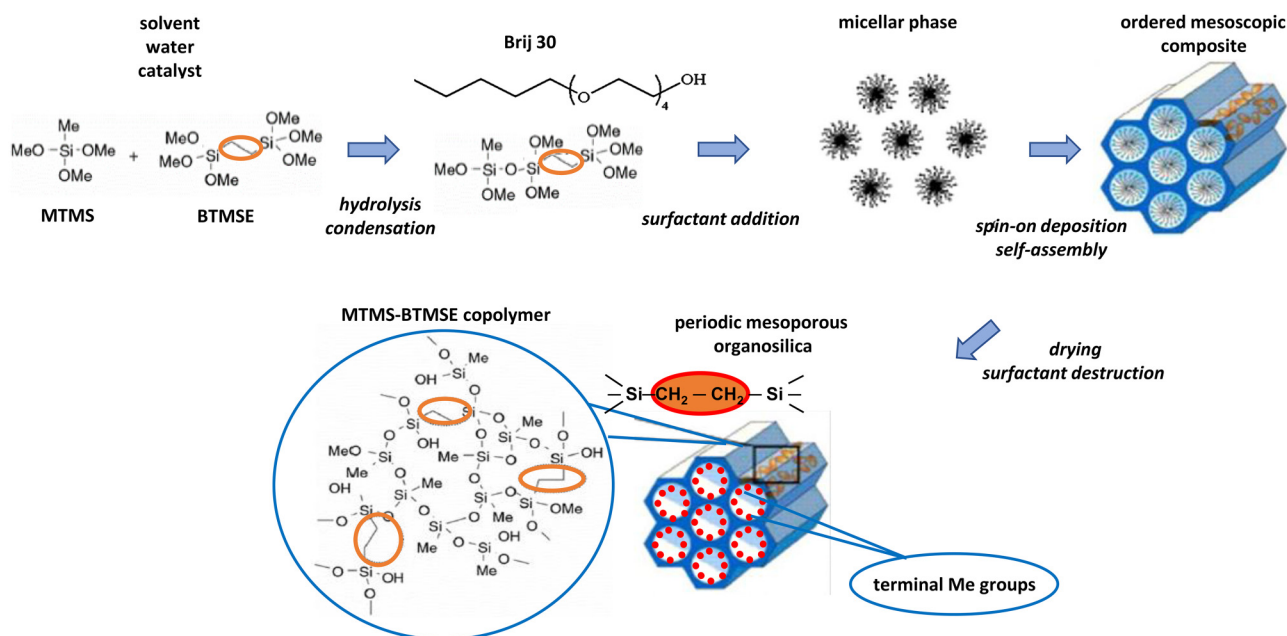

FIG. 1. Schematic pathway of the formation of the ethylene bridged PMO film from MTMS and BTMSE precursors and the Brij 30 template.

measured at room temperature without an analysis of phonon-assisted charge transport mechanisms. In fact, the Frenkel mechanism is commonly used to describe the dielectric conductivity but without analyzing the pre-exponential frequency factor value, which, in the most of cases, is underestimated, compared to the theoretical value of W/h (W, trap energy; h, Planck constant). Therefore, the Frenkel mechanism, formally, can describe the charge transport in SiO_2, Si_3N_4, and some high-κ oxides; however, qualitatively and quantitatively, the conductivity of these dielectrics is described within phonon-assisted models, such as multiphonon ionization of neutral traps at low trap concentrations (Si_3N_4, Al_2O_3) and the model of phonon-assisted tunneling between neutral traps at their high concentrations (SiO_2, HfO_2, Ta_2O_5, Sc_2O_3).[20–25]

The current–voltage characteristics of porous PECVD low-κ dielectrics without the comparison of experimental data and theoretical models of the charge transport mechanism were reported in the paper.[26] A high concentration of electron traps in the dielectric, leading to the hysteresis of capacitance–voltage characteristics and current relaxation with time, was found. The charge transport in most of the oxide-based dielectrics is substantially determined by intrinsic defects such as oxygen vacancies. The oxygen vacancies in SiO_2 and many high-κ oxides act as traps for the charge carriers.[22–25] One can assume that the oxygen vacancies in a low-κ dielectric also play an important role for the dielectric leakage current.

Thus, the aim of the current study is to investigate the electronic structure, the charge transport mechanism, and the nature of the traps responsible for the conductivity of new ethylene bridged periodic mesoporous organosilica low-κ dielectric films. It was assumed that the presence of the ethylene bridge between silicon atoms can result in significantly different behavior of electrically active defects and properties of a low-κ material.

II. MATERIALS AND METHODS

The OSG low-κ dielectric films were fabricated by chemical solution deposition using the evaporation-induced self-assembly (EISA).[27] The film-forming solution was prepared by cohydrolysis of 1,2-Bis(trimethoxysilyl)ethane (BTMSE, 96%, Aldrich) with methyltrimethoxysilane (MTMS, >98%, Fluka) in tetrahydrofuran (THF, anhydrous, 99.9%, Sigma-Aldrich) at acidic conditions (hydrochloric acid, HCl, ACS reagent 37%; Sigma-Aldrich was used as a catalyst). A mixture of MTMS, BTMSE, HCl, and H_2O in THF was stirred at 60 °C. The molar ratio of BTMSE/MTMS was 45/55. The Brij30 surfactant $[C_{12}H_{25} (OCH_2OCH_2)_4OH$ with a molar mass of 362 g/mol, for R&D, Sigma-Aldrich] was added as the structure directing agent to the resulting solution of the organosilica precursors. During the EISA process, excess of solvent ensures that the initial concentration of the surfactant remains below the critical micelle concentration. During the solvent evaporation, the surfactant concentration transcends the critical micelle concentration, and the surfactant forms micellar aggregates (self-assembling). The micellar aggregate serves as a template for the polycondensation of the precursor molecules in an ordered mesoscopic composite and can be removed by a thermal treatment, leaving behind a porous PMO material (Fig. 1). The role of MTMS is the introduction of terminal methyl groups that are necessary to achieve sufficient thermal self-hydrophobization. The methyl groups are preferentially located on the pore wall surface after the heat treatment.[28]

The spin-on deposition was performed by using a WS-650-8NPP (Laurell, USA) spin coater at the rotation speed of 2500 rpm. Standard p-type silicon wafers (doped with boron, resistivity—12 Ω/cm) with a diameter of 100 mm and a (100) orientation were used as substrates. After deposition, the films were soft baked on a hot plate at $T = 150–200$ °C for 10 min to complete solvent evaporation and then hard baked in an oven at 400–430 °C for 30 min in the air to remove the organic residues and to complete polycondensation reactions.

The optical properties and film thicknesses were determined by a spectroscopic ellipsometer ELLIPS-1891-SAG. The ellipsometric characteristics were measured in the photon energy range of 1.13–4.50 eV with a device spectral resolution of ∼0.01 eV. The light beam incidence angle on the sample was 70°. A four-zone measurement technique was used, followed by the averaging over all zones. An optical model of a single layer reflecting system was used. The calculations showed the absence of the light absorption in low-κ films in the studied spectral region. Thus, the film thicknesses and the $n(E)$ were calculated based on the Cauchy polynomial function. For calculations, the optical characteristics of Si were taken from Ref. 29.

The surface mapping of the low-κ dielectric deposited on the silicon wafers of 150 mm in diameter was made by means of scanning ellipsometry with a high spatial resolution [MICROSCAN (ISP SB RAS)].[30] The scanning step (x, y) was 3 mm. The ellipsometer consists of a high-stable He–Ne (633 nm, 1 mW) laser as a light source. The laser beam was focalized into the 10 nm light spot with a high-quality non-polarizing micro-objective. The ellipsometer is equipped with the computer operated scanning stage that allows one to measure the optical parameter distribution over the sample surface up to 150×150 mm^2.

The film porosity and pore size distribution were measured using atmospheric pressure ellipsometric porosimetry.[31,32] Heptane vapor was used as an adsorptive. The films' open porosity is calculated as the volume of the adsorbed liquid (adsorptive) from the values of refractive indices (RIs) measured during the heptane adsorption by using the Lorentz–Lorenz equation,

$$\frac{n_{eff}^2 - 1}{n_{eff}^2 + 2} = V \frac{n_{ads}^2 - 1}{n_{ads}^2 + 2} + (1 - V) \frac{n_s^2 - 1}{n_s^2 + 2}, \quad (1)$$

where n_{eff} is the measured RI of the porous film when the pores are partially or completely filled by an adsorptive, n_{ads} is the RI of a liquid adsorptive, n_s is the skeleton RI, and V is the volume of the condensed adsorptive (open porosity). In the case of OSG films, the skeleton RI is normally close to the refractive index of amorphous SiO_2 ($n = 1.46$). The calculation of the pore radius distribution (PRD) is based on an analysis of adsorption isotherms and hysteresis loops that appear due to the difference in the curvature radius of the condensed liquid meniscus during the adsorption and desorption. The pore radius calculation uses the Kelvin equation that describes the dependence of the relative pressure (P/P_o) on the meniscus curvature.

The electronic structure of thermal SiO_2 and nonstoichiometric $SiO_{x<2}$ was also studied as reference samples for the comparison

with the OSG low-κ dielectric. A SiO_x film was synthesized by the PECVD method from the SiH_4–O_2 gas mixture under an inductive high-frequency excitation as is described previously.[33]

The bulk chemical composition of the deposited low-κ films was analyzed by using Fourier-Transform Infrared spectroscopy (FTIR Nicolet 6700, Thermo Scientific). The near surface region composition of the samples was elucidated by X-ray photoelectron spectroscopy (XPS) using a SPECS photoelectron spectrometer with a PHOIBOS-150-MCD-9 analyzer and a FOCUS-500 monochromator (Al Kα radiation, $h\nu = 1486.74\,eV$, 200 W). The XPS spectra were recorded at the constant take-off angle of 900. The peak's binding energy (BE) was calibrated by the C1s peak position (284.8 eV) corresponding to surface hydrocarbon-like deposits. The film surface was etched with Ar^+ ions with the energy of 1.25 keV at the current density of 8–$10\,\mu A\,cm^{-2}$ for 10 min using an IQE 11/35 ion gun. The depth profiling rate under these conditions was estimated as 0.5 nm/min. The Ar^+ etching was considered as a method of metal cations' partial reduction and of oxygen vacancy generation as it was observed in SiO_2 films.[34] The electron energy loss spectra (EELS) were recorded on the Auger spectrometer Riber LAS-2000 with the energy of a primary monochromatized electron beam 200.5 eV and the signal modulation amplitude on the synchronous detector 0.3 V. The photoluminescence of the films was measured on Jasco FP-8300. An Xe lamp was used as a light source, and the excitation and emission spectra range were in the wavelength from 200 to 750 nm.

Metal (Mg) contact with a size of $0.5\,mm^2$ was sputter deposited on top of a low-κ dielectric with a porosity of 35.8% and a k-value of 2.3 using a shadow mask. A continuous Al layer was sputtered on the backside of the Si wafer. For outgassing and the removal of adsorbed residues, the low-κ layer was annealed at 300 °C in Ar just before the metal contact deposition. The current–voltage characteristics of p-Si/low-κ/Mg structures were measured at temperatures of 300 K, 310 K, 320 K, and 330 K at the negative potential on the

Mg electrode using the Keithley 2400 equipment. The voltage ramp rate in the current–voltage characteristic measurement was $0.9\,V\,s^{-1}$.

The simulation of α-SiO_2 and $SiO_{x<2}$ electronic structures was carried out in the Quantum ESPRESSO package within the density functional theory (DFT).[35] The PBE0 functional was used to provide the SiO_2 bandgap value of 8.0 eV.[22] The cutoff energy for the plane waves was 950 eV, and the core was described through norm-conserving pseudopotentials. The SiO_x structure was modeled by the removal of oxygen atoms from a 36-atom SiO_2 supercell followed by structural relaxation. The oxygen atoms were removed on the principle of minimum formation energy.[36] The XPS valence band was calculated by summing up the projected density states (PDOS) with the weight factors obtained from the best agreement of calculations and experiments for SiO_2 and with the broadening by the Gauss function (σ = 0.6 eV).

III. RESULTS AND DISCUSSIONS

A. Chemical composition and porous structures

The bulk chemical composition of the deposited films was evaluated by using FTIR spectroscopy. Figure 2 shows FTIR spectra of the deposited films. The observed spectra are typical for OSG films.[37,38] In addition to Si—O—Si groups with the most intensive peak related to stretching vibrations located at 1100–1000 cm^{-1}, the terminal Si—CH_3 bonds (bending vibrations at 1280–1270 cm^{-1}) is an important component providing the films' hydrophobicity. The absorption peaks from the organic template residues and C—H vibrations from Si—CH_3 groups are located between 3000 and 2800 cm^{-1}. The ethylene bridging groups originated from the BTMSE precursor (Fig. 1) are not very pronounced in FTIR spectra because of their non-polar nature. Their analysis can be based on the peaks located in different parts of FTIR spectra: the peaks located near 1415 cm^{-1} [bending dCH_2 vibration in Si—$(CH_2)_2$—Si], (—CH_2—CH_2—) rocking vibration at 715 cm^{-1}, and 2895 and
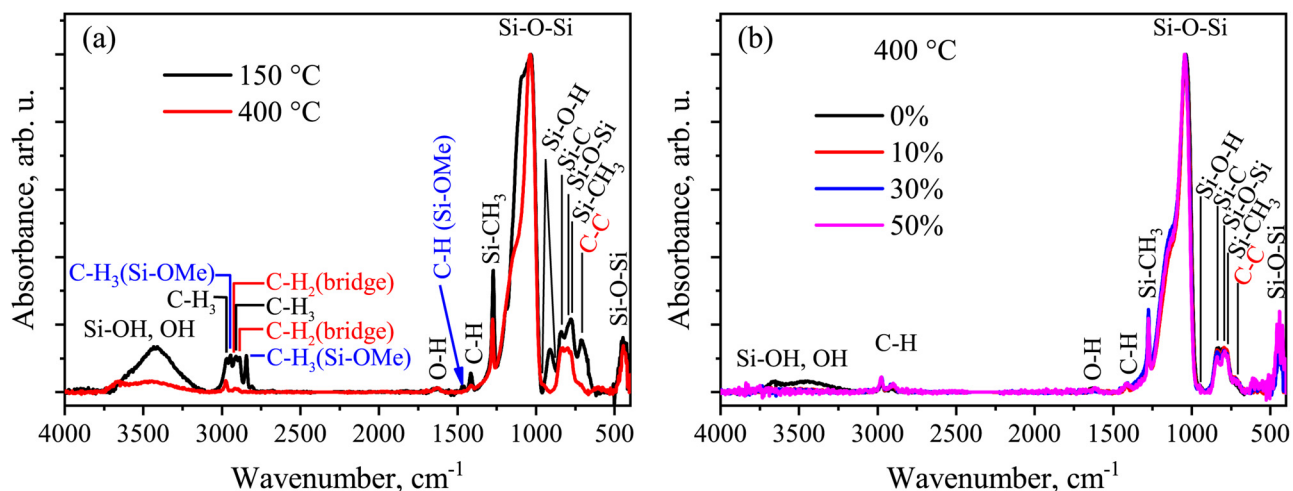
FIG. 2. FTIR spectra of the deposited OSG films. Comparison of soft and hard baked films deposited without surfactants (a) and FTIR spectra of fully cured films deposited with different surfactant concentrations (b).
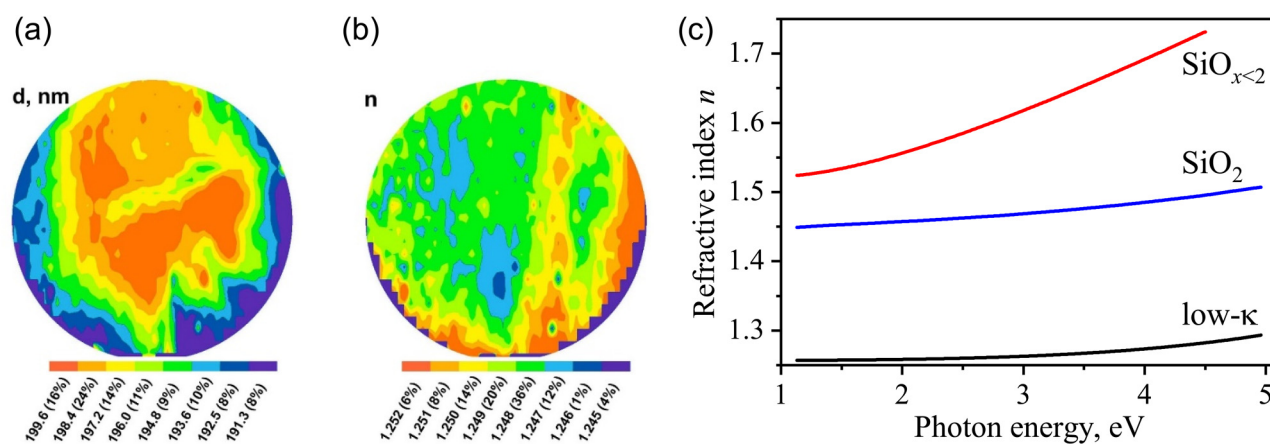
FIG. 3. Ellipsometric map of a 196 nm thick low-κ dielectric film surface (RI = 1.249). The mapping parameters: (a) thickness d and (b) refractive index n. (c) Refractive index dispersion for the PMO low-κ, SiO$_2$, and SiO$_{x<2}$ films.

2925 cm^{-1} (ν_s and ν_{as} of C—H in the CH$_2$ group) (see Figs. S1–S3 in the supplementary material). As can be seen from Fig. 2(a), the soft baked film is still hydrophilic and contain significant amount of adsorbed water (3000–3750 cm^{-1}). Also, the template aggregates and silica precursors are not completely removed as we can see from the CH$_x$ and Si—OMe peaks at 2700–3000 cm^{-1}. The hard bake at 400 °C removes the adsorbed water and template residues. The final composition of the completely cured films is almost independent on the template concentration, but the films deposited without the template are more hydrophilic [Fig. 2(b)].

According to an ellipsometric analysis, the studied low-κ films deposited onto Si wafers had a high homogeneity in the thickness and refractive index (Fig. 3). The film thickness decreases, and the

refractive index slightly grows up from the center to the wafer edge, which is typical for spin-on deposition of alkoxide based sols and usually associated with the non-Newtonian liquid rheology.[39,40]

It was mentioned that the SiO$_2$ (120 nm) and SiO$_x$ (210 nm) films were used as references. The refractive index dispersion spectrum $n(\hbar\omega)$ is monotonically increasing, and it is typical for dielectrics in the $\hbar\omega$ range values less than that of the dielectric bandgap E_g. The low-κ dielectric dispersion spectrum curve is almost parallel to the ones for the SiO$_2$. Thus, the E_g values of a low-κ dielectric, as well as SiO$_2$, are greater than the measurement range, i.e., 5 eV.

Figure 4 shows the results of porosity evaluation. According to Fig. 4(a), the film deposited without a surfactant does not show the presence of open pores (dense), the films deposited with 10%
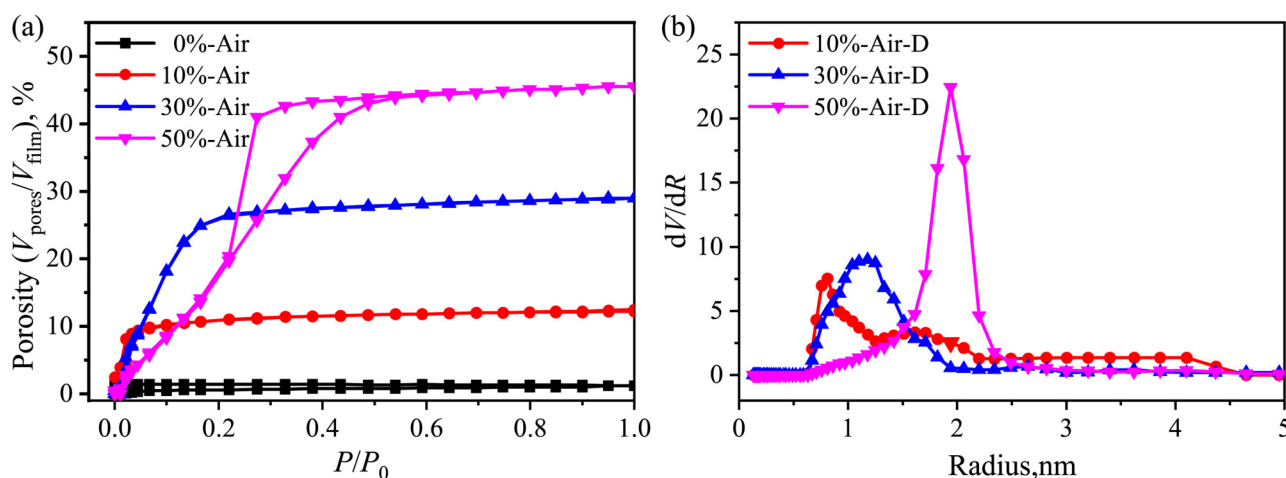

FIG. 4. Adsorption–desorption isotherms of heptane vapors in the films deposited with different template concentrations (a) and pore size distributions in these films (calculated from the desorption curve) (b).

and 30% of the template have porosity that well correlates with the template concentration, and the isotherms do not have a hysteresis loop. The film deposited with 50% of the template have quite a different isotherm. First, porosity is slightly smaller than the template concentration (45% against 50%), and the isotherm has a pronounced hysteresis loop. A significant difference between the adsorption and desorption branches suggests formation of internal voids with the size larger than the size of interconnecting necks. Such behavior is normally termed as the formation of ink-bottle types of pores.[10] Figure 4(b) presents the pore radius distribution calculated from the desorption curves. One can see that the pore radius increases with porosity (from 0.8 nm for the film deposited with 10% of porogen to 1.2 nm for 30% and 2 nm for the film deposited with 50% of porogen).

B. States of oxidation and internal defects

In the XPS Si2p spectra of PMO low-κ and SiO$_2$ samples, the signal from Si^{4+} oxidation states with the binding energy of 103.5 eV is dominated [Fig. 5(a)]. The low-energy broadening of the Si2p spectra for the low-κ dielectric could be explained by the organic content leading to the formation of Si—C bonds ($\equiv$Si—CH$_3$ and $\equiv$Si—CH$_2$—CH$_2$—Si$\equiv$).[41,42] The low-energy shoulder for a low-κ sample (Fig. 5) qualitatively looks like that of the SiO$_{x<2}$ one and can also be deconvoluted into different silicon oxidation states: Si^{1+}, Si^{2+}, and Si^{3+}.[43] The presence of Si^{3+} and Si^{2+} oxidation states can be interpreted as the presence of so-called T-groups [one methyl group bonded to an Si atom, O$_3$Si(CH$_3$)] and D-groups [=O$_2$Si(CH$_3$)$_2$] that for the first time were observed by nuclear magnetic resonance in i-CVD OSG films.[44] For the studied SiO$_{x<2}$ film, the [O]/[Si] atomic ratio (x), as calculated from the integral photoelectron peak intensities corrected with the relative sensitivity factors, is about 1.2.

The high-energy broadening was previously interpreted as a signal from the Si—OH group.[41,42] It could also be caused by the positive charging of organic components when the matter was irradiated with x-ray quanta. An alternative possibility of positive charging is the presence of Si—Si bonds. The Si—Si bond in SiO$_2$ can localize both electrons and holes, but the hole capturing probability is much greater than the electron one, since the electron capture cross section on the Si—Si bond $\sigma_e = 10^{-15}$ cm^{-2} is much less than that for the hole $\sigma_h = 10^{-1}$ cm^{-2}.[45] Under x-ray irradiation, holes generated in the dielectric can be captured on the Si—Si bond, leading to the positive charge accumulation. In turn, this leads to the increase of the Si2p atomic level binding energy.

The bombardment by Ar$^+$ ions is accompanied by a small Si2p level broadening mainly to the low-energy region for both the low-κ dielectric and SiO$_2$ samples [Fig. 5(b)]. This is due to the formation of oxygen vacancies by knocking out oxygen atoms from $\equiv$Si—O—Si$\equiv$ bridges and to those previously reported for SiO$_2$ and TiO$_2$.[34,46]

The valence band for the PMO low-κ dielectric agrees surprisingly well with that for SiO$_{1.2}$ [Fig. 6(a)]. The discrepancy is observed only for the valence band top, which is shifted to the bandgap for SiO$_x$, compared to the low-κ dielectric. In turn, for both the low-κ dielectric and SiO$_{1.2}$, there is the valence band top shift to the low-energy region in comparison with stoichiometric SiO$_2$. For SiO$_2$, the XPS shows a shoulder in the low-energy region after the Ar$^+$ ion bombardment. It is caused by oxygen vacancies, as seen from the comparison with the calculated XPS for perfect and oxygen-depleted SiO$_2$. The oxygen vacancies in SiO$_2$ give the filled defect states near the oxide valence band top formed by Si3p and Si3s atomic orbitals [Fig. 6(b)]. These states correspond to the binding σ-orbitals of Si—Si bonds.[47,48] The Ar$^+$ ion bombardment of a low-κ dielectric film leads to a similar valence band top broadening. Thus, it can be assumed that the low-energy broadening of the valence-band edge for the PMO low-κ dielectric, as well as for SiO$_x$ in comparison with SiO$_2$ is caused by Si—Si bond formation, and their concentration increases after the Ar$^+$ ion bombardment.
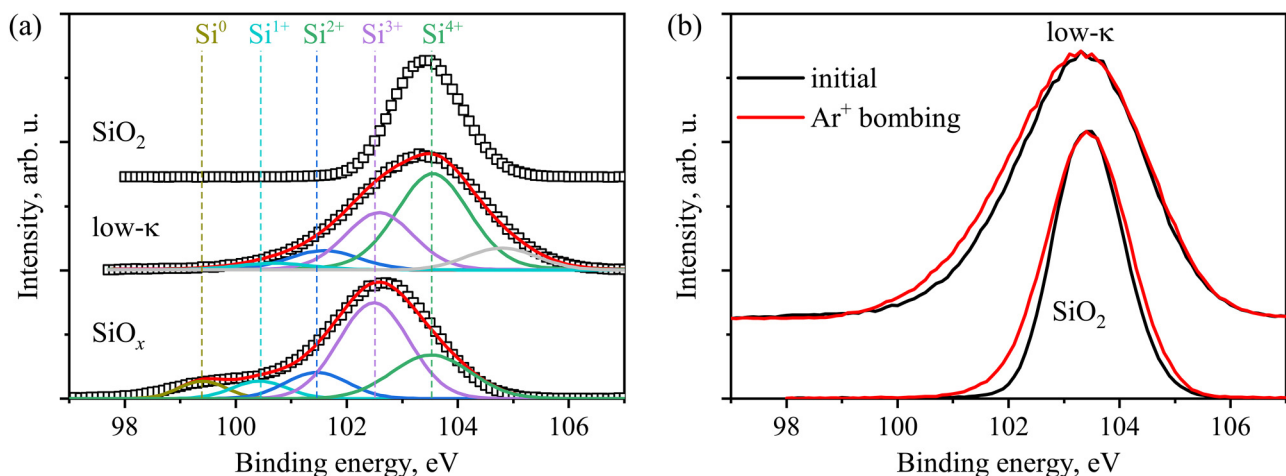

FIG. 5. (a) XPS Si2p spectra (symbols) and the deconvolution (colored lines) of low-κ, SiO$_2$, and SiO$_x$. (b) XPS Si2p spectra for the initial (black lines) and after the Ar$^+$ ion bombardment (red lines) of low-κ and SiO$_2$ samples.
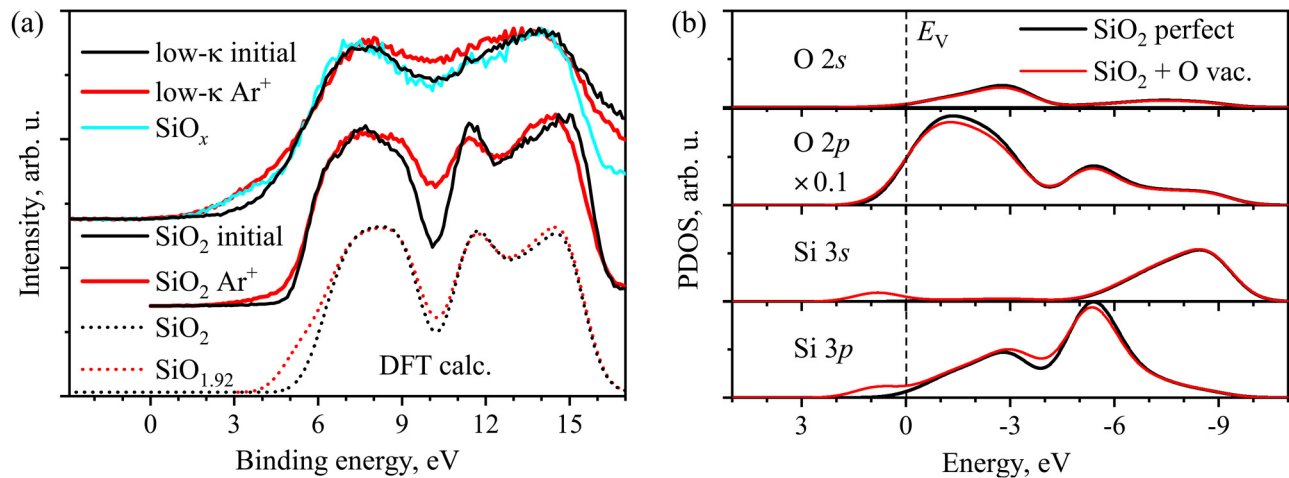
FIG. 6. (a) Valence band XPS spectra of a low-κ dielectric, SiO₂, and SiOₓ before and after Ar⁺ ion bombardment. The dotted curves are the theoretical XPS spectra of perfect SiO₂ and SiO₂ with O vacancies (1 vacancy per 36 atoms). (b) Calculated PDOS spectra for perfect and defect SiO₂.

The above-mentioned discrepancy for a low-κ dielectric and $SiO_{1.2}$ is due to that the last one is highly enriched with silicon, and it should have a greater Si—Si bond concentration. It is necessary to mention that silicon-dangling bonds (E'-center) and carbon-related centers have also been detected in the porous methyl terminated OSG low-κ dielectric using the Electron Spin Resonance (ESR) method.[49]

The O1s spectrum for the PMO low-κ dielectric is broadened compared with those for SiO₂ and SiOₓ, while the binding energies of O1s electrons for all dielectrics coincide and are equal to 532.5 eV [Fig. 7(a)]. The broadening could be explained by the presence of hydroxyl and not completely hydrolyzed methoxy

groups from the precursors. The bulk plasmon energy $\hbar\omega_B$ for the PMO low-κ dielectric of 21.7 ± 0.3 eV is very close to the one for SiOₓ. This independently indicates the similarity of their electronic structures. Previously, the value $\hbar\omega_B = 22.1$ eV was obtained for the PECVD low-κ dielectric.[50] The bulk plasmon energies for SiO₂ and SiOₓ (about 22.3 and 21.5 eV, respectively) are in a good agreement with the known values.[50–52] Our data obtained for PECVD SiOₓ confirm the weak dependence of $\hbar\omega_B$ on the x value (when 1<x<2), as earlier established for SiOₓ prepared by the dc sputtering of an Si target in an oxygen mixture.[51]

The O1s XPS also reflects the photoelectron energy loss spectrum since photoelectrons lose part of their kinetic energy at
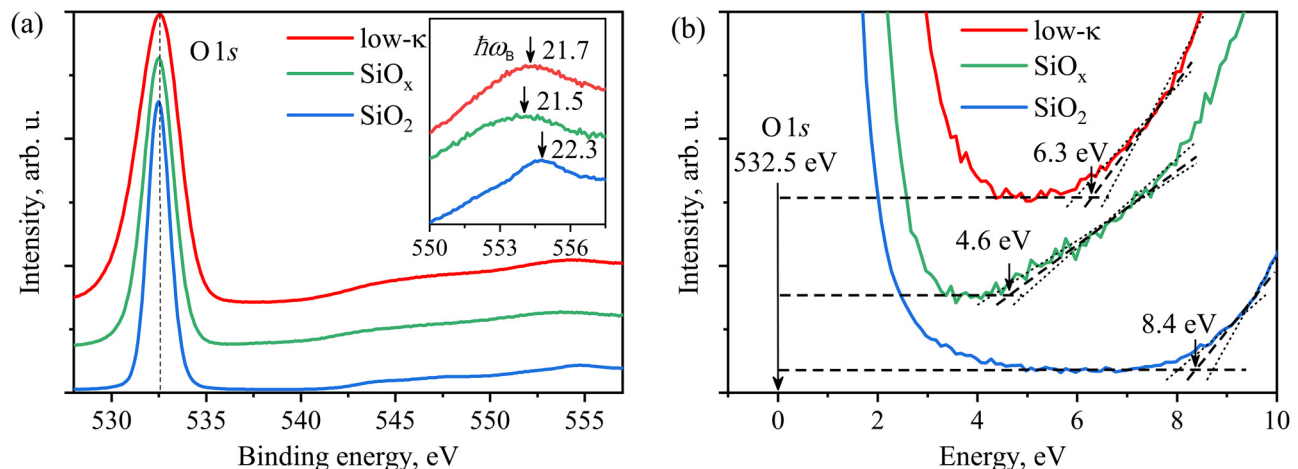

FIG. 7. (a) XPS O1s spectra of low-κ dielectric, SiO₂, and SiOₓ samples. (b) O1s photoelectron energy loss spectra and measurements of the low-κ dielectric, SiO₂, and SiOₓ bandgap values.
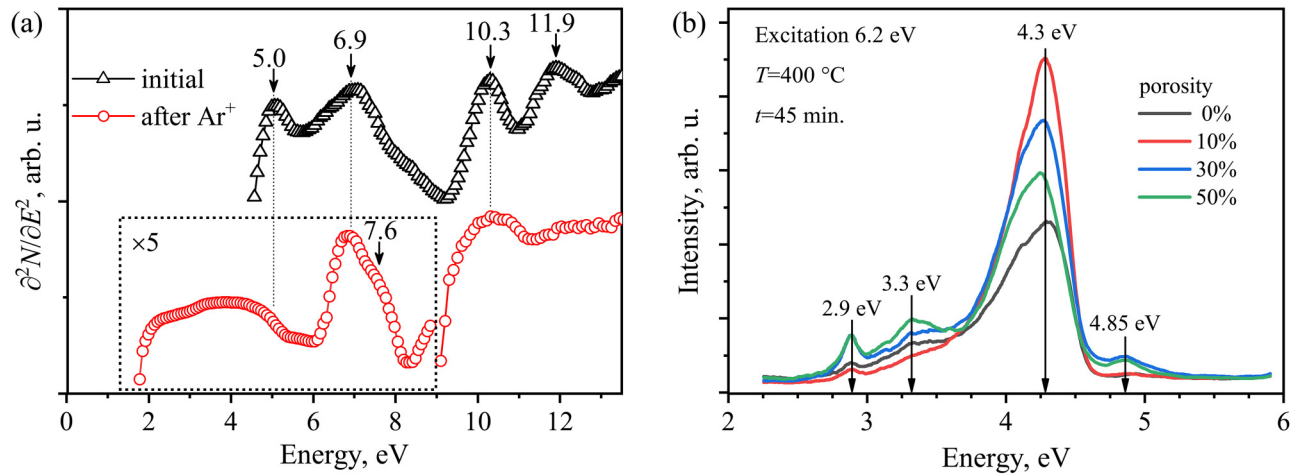
FIG. 8. (a) EELS of the PMO low-κ dielectric for the initial state of the surface and after the Ar⁺ ion bombardment with the energy of 3 keV for 15 min. (b) UV induced photoluminescence of OSG films with different porosities.

interband electronic transitions [Fig. 7(b)]. Thus, the onset of the band-to-band transition excitation corresponding to the bandgap energy value E_g can be found using a linear interpolation of the photoelectron loss spectrum edge to the background level [Fig. 7(b)]. This procedure yields the bandgap values of 6.3 ± 0.3 eV, 8.3 ± 0.3 eV, and 4.6 ± 0.3 eV for the PMO low-κ dielectric, SiO_2, and $SiO_{x<2}$, respectively. The error values are caused by the arbitrariness in the selection of the energy range for linear interpolation. The E_g value obtained for the PMO low-κ dielectric falls on the lower limit of the values ranging from 6 to 9 eV, which can be found in the literature for the OSG low-κ dielectric film.[50,53–55] This can be explained by the fact that the studied films are characterized by a relatively high defect state density near the low-κ dielectric valence-band edge, which leads to photoelectron energy loss peak broadening toward a lower binding energy. The E_g for SiO_2 is consistent with the calculated one for α-SiO_2 ($E_g = 8.0$ eV), and the experimental values range from 8.0 to 9.0 eV.[56–59]

The second derivative of the EELS (spectra of inelastic scattered electrons with the energy of 205 eV) of a PMO low-κ dielectric exhibits an intense peak with the energy of 6.9 eV for both the initial film and the film after the Ar⁺ ion bombardment [Fig. 8(a)]. The excitation with an energy of about 6.9 eV for SiO_2 is accepted to refer to the triple silicon cluster Si—Si—Si (or oxygen divacancy).[60–62] After Ar⁺ ion bombardment, the features at the energy range of 2–5 eV and a shoulder with the energy of 7.6 eV are observed. The 7.6 eV excitation energy is most likely related to the presence of Si—Si bonds (oxygen vacancy) as it is valid for SiO_2.[61–65] Thus, EELS spectroscopy data confirm the presence of defects in the studied low-κ dielectric film associated with excess silicon. Low-energy excitations with energies in the range of 2–5 eV could be explained by electronic transitions on oxygen tri-vacancies, silicon vacancies, or their combination with the organics.[63,66]

The presence of oxygen deficient centers in ethylene bridged PMO films has also been confirmed by the study of UV induced

luminescence [Fig. 8(b)].[67] The luminescence in these experiments has been induced by 200 nm UV light. Three peaks observed in the spectra can be interpreted as related to oxygen-deficiency-related centers (≈ 4.3 eV),[61] some remaining silanol groups (≈ 3.3 eV), and to the presence of carbon- and/or oxygen-type defects (≈ 2.9 eV).[68] It is important that the oxygen-deficiency-related peaks are the most intensive and has the highest intensity in the films with 10% of porosity. These films have the smallest pore size (Fig. 4) and, therefore, the highest internal surface area. Therefore, one can assume that these kinds of defects are mainly located on the pore wall.

Therefore, the results obtained by XPS and UV induced luminescence suggest the presence of oxygen-deficiency-related centers. It is reasonable to assume that these centers can recombine forming Si—Si bonds. We tried to detect the presence of Si—Si bonds in the studied PMO low-κ dielectric films from the analysis of Raman spectra obtained with the Raman spectrometer T64000 (the experimental setup was described previously[69]). However, there are no peaks of wave numbers about 480 cm⁻¹ corresponding to Raman scattering on the local vibrations of Si—Si bonds in the spectra.[70] It can be concluded that the Si—Si bond concentration in the film is less than the method detectability, which, in this case, is no more than 3 at. % according to our estimates. In addition, it can be stated unequivocally that there are no silicon clusters with a size greater than 2 nm in the studied films.

C. Results of electrical evaluation

Figure 9 shows the current–voltage characteristic at different temperatures (j–F–T) measured by using experimental p-Si/PMO-low-κ-dielectric/Mg structures and their fitting with different charge transport models. To establish the PMO low-κ charge transport mechanism, we examined six most likely temperature-dependent models where the transport is limited by trap ionization: Frenkel,[71,72] Hill–Adachi,[73,74] Shklovskii–Efros,[75,76] Makram-Ebeid
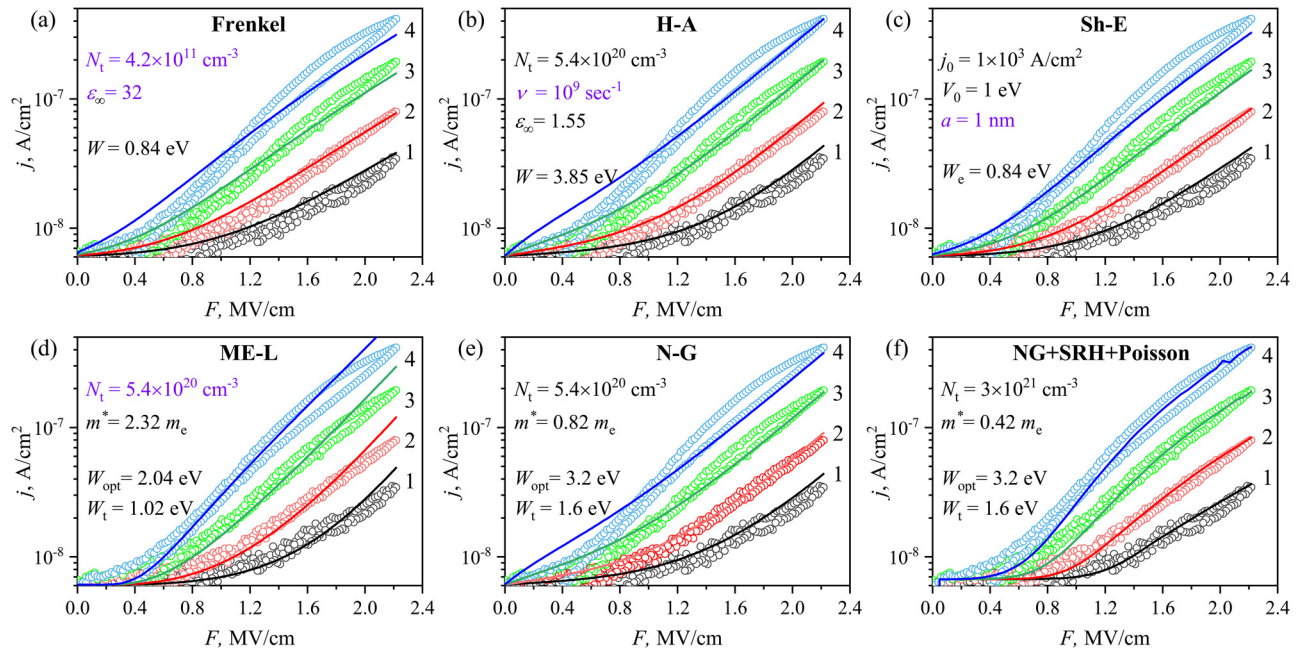
FIG. 9. Experimental (characters) and simulation (solid lines) current–voltage characteristics of the p-Si/low-κ dielectric/Mg structures at 300 K (1), 310 K (2), 320 K (3), and 330 K (4): (a) the Frenkel model, (b) the Hill–Adachi (H–A) model, (c) the Shklovskii–Efros (Sh–E) model, (d) the Makram-Ebeid and Lannoo (ME–L) model, (e) the Nasyrov–Gritsenko (N–G) model, and (f) the Nasyrov–Gritsenko model considering the space charge and Shockley–Read–Hall (SRH) recombination (N–G + SRH + Poisson). Model parameters are included in the figures.

and Lannoo (ME–L),[77] Nasyrov–Gritsenko,[78] and Nasyrov–Gritsenko considering the space charge and Shockley–Reed–Hall (SRH) recombination.[79] The Frenkel mechanism assumes thermal ionization of an isolated Coulomb trap in the electric field that reduces the energy barrier. In the Hill–Adachi model, the ionization barrier energy is reduced by overlapping two adjacent Coulomb traps. The Shklovskii–Efros model for fluctuating potentials assumes the delocalization of electrons with the energy above the percolation energy and their movement in a random potential in an external field. According to the Makram-Ebeid and Lannoo model, the charge transport in a dielectric is governed by the multi-phonon ionization of isolated charged traps. In the Nasyrov–Gritsenko model, the act of charge transfer occurs via the phonon-assisted electron tunneling between the neighboring neutral traps without their excitation to the conduction band. The current density j through the material containing traps is the sum of the drift current and the displacement current. The drift current is defined by the equation

$$j_{dr} = eN_t Pl \approx eN_t^{2/3} P, \qquad (2)$$

where N_t is the filled trap concentration, P is the probability (rate) of the electron emission from traps per second, and l is the electron free path to the next capture on the trap, which can be considered approximately equal to the average distance between the traps s

($l \approx s = N_t^{-1/3}$). The expressions of the drift current for different charge transport models are presented in Table I.

The fitting by the Frenkel model yields an acceptable value of W, but the N_t value necessary for fitting by using $\nu = W/h$ is abnormally small and ε_∞ is nonphysically large [Fig. 9(a)]. Hence, it is safe to say that the Frenkel model is not suitable to describe the PMO low-κ dielectric charge transport. The Hill–Adachi model qualitatively describes the experimental j–F–T characteristic at reasonable N_t, ε_∞, and W values but at an abnormally low (by about 6 orders of magnitude) value of the attempt-to-escape frequency ν, which should be close to $W/h \sim 10^{14}\,\text{s}^{-1}$ [Fig. 9(b)]. Consequently, the H–A model does not describe the charge transport mechanism in the PMO low-κ dielectric too. When describing the experimental data by the Shklovskii–Efros model, the spatial scale of the potential fluctuation is obtained equal to 1 nm [Fig. 9(c)]. Such a small scale means a high tunnel transparency of potential barriers for charge carriers; therefore, the classical Shklovskii–Efros percolation model is not applicable. The Makram-Ebeid and Lannoo model of isolated charged traps can be used to qualitatively describe the PMO low-κ current–voltage characteristic at reasonable W_t, W_{opt}, and m^* values [Fig. 9(d)]. However, the N_t value is too high for the ME–L model, since it corresponds to the small average distance between the traps at $s \approx 1.2\,\text{nm}$, which causes the preferable electron tunneling between neighboring traps, instead of ionization into the conduction band. It is concluded that the ME–L model is also not suitable to describe the PMO low-κ dielectric charge transport.

TABLE I. Expressions for the charge transport models in dielectrics. Here, F is the electric field, T the temperature, k the Boltzmann constant, e the electron charge, ε_0 the vacuum permittivity, ε_∞ the high-frequency permittivity, j_0 the preexponential factor, V_0 the energy fluctuation amplitude, a the fluctuation space scale, I_n the modified Bessel function, m^* the electron effective mass, $\hbar = h/2\pi$ the Planck constant, W_e the percolation energy, W_{ph} the phonon energy, W the trap energy, W_t the thermal trap energy, W_{opt} the optical trap energy, ν the attempt to escape factor, and υ the drift velocity.

Model	Equation	Fitting parameters
Frenkel	$j_{dr} = eN_t s\nu \exp\left(-\dfrac{W - \beta_F \sqrt{F}}{kT}\right), \quad \beta_F = \left(\dfrac{e^3}{\pi\varepsilon_\infty\varepsilon_0}\right)^{1/2}, \quad \nu = \dfrac{W}{h}$	N_t, ε_∞, W
Hill–Adachi	$j_{dr} = 2eN_t s\nu \exp\left(-\dfrac{W - \frac{e^2}{\pi\varepsilon_\infty\varepsilon_0 s}}{kT}\right)\sinh\left(\dfrac{eFs}{2kT}\right)$	N_t, ν, ε_∞, W
Shklovskii–Efros percolation	$j_{dr} = j_0 \exp\left(-\dfrac{W_e - (0.25eFaV_0^{0.9})^{\frac{1}{1+0.9}}}{kT}\right)$	j_0, V_0, a, W_e
Makram-Ebeid and Lannoo	$j_{dr} = eN_t s \displaystyle\sum_n \exp\left(\dfrac{nW_{ph}}{2kT} - \dfrac{W_{opt} - W_t}{W_{ph}}\coth\dfrac{nW_{ph}}{2kT}\right) I_n\left(\dfrac{W_{opt} - W_t}{W_{ph}\sinh(W_{ph}/2kT)}\right) P_i$ $P_i = \dfrac{eF}{2\sqrt{2m^*(W_t + nW_{ph})}}\exp\left(-\dfrac{4}{3}\dfrac{\sqrt{2m^*}}{\hbar eF}(W_t + nW_{ph})^{3/2}\right)$	N_t, W_t, W_{opt}, m^*
Nasyrov–Gritsenko	$j_{dr} = \dfrac{2eN_t\sqrt{\pi}\hbar W_t}{m^* s\sqrt{2kT(W_{opt} - W_t)}}\exp\left(-\dfrac{W_{opt} - W_t}{kT}\right)\exp\left(-\dfrac{2s\sqrt{2m^* W_t}}{\hbar}\right)\sinh\left(\dfrac{eFs}{2kT}\right)$	N_t, W_t, W_{opt}, m^*
Nasyrov–Gritsenko with Poisson and Shockley–Reed–Hall equations	$j_{dr} = eN_t s \displaystyle\int \dfrac{\hbar|E|}{m^* s^2 kTQ_0}\exp\left\{-\left(\dfrac{(Q - Q_0)^2 + (Q - eFs/Q_0)^2}{2kT} - \dfrac{4\sqrt{2m^*}}{3\hbar eF}[(E)^{3/2} - (E - eFs)^{3/2}]\right)\right\}dQ$ $E = Q_0(Q - Q_0) + W_{opt}; \quad Q_0 = \sqrt{2(W_{opt} - W_t)}$ $\begin{cases} \dfrac{\partial n(x,t)}{\partial t} = -\upsilon\dfrac{\partial n(x,t)}{\partial x} - \sigma\upsilon n(x,t)(N_t^e - n_t(x,t)) + n_t(x,t)P_{ion}(x,t) \\ \dfrac{\partial n_t(x,t)}{\partial t} = \sigma\upsilon n(x,t)(N_t^e - n_t(x,t)) - n_t(x,t)P_{ion}(x,t) \\ \dfrac{\partial F(x,t)}{\partial x} = -e\dfrac{n_t(x,t)}{\varepsilon\varepsilon_0} \end{cases}$	N_t, W_t, W_{opt}, m^*

The Nasyrov–Gritsenko model correctly represents the experimental j–F–T characteristics, both qualitatively and numerically [Fig. 9(e)]. The $W_t = 1.6$ eV and $W_{opt} = 3.2$ eV values are in excellent agreement with the reported trap energies in SiO_2, and the traps with the specified W_t and W_{opt} energies in SiO_2 are Si—Si bonds.[22] Since the presence of excess silicon was shown for the studied PMO low-κ dielectric films, it can be concluded that the charge transport through them occurs via the phonon-assisted electron tunneling between the neighboring neutral traps and that traps are Si—Si bonds.

One can see that the model of phonon-assisted electron tunneling between the traps considering the space charge and trap-assisted charge recombination describes the charge transport over the entire field range much better [Fig. 9(f)]. At the same W_t and W_{opt} values, the N–G + SRH + Poisson model describes the experiment at $m^* = 0.42\ m_e$, which is very close to the tunnel effective mass value in SiO_2.[80] At the same time, this model gives a noticeably higher trap concentration value N_t, compared with the simple Nasyrov–Gritsenko PATT model.

IV. CONCLUSION

Organosilicate-glass-based low-κ films containing both terminal methyl groups and an ethylene bridge between silicon atoms are spin-on deposited by using 1,2-bis(trimethoxysilyl)ethane (BTMSE) and methyltrimethoxysilane (MTMS), Brij30 template, and thermal curing. The chemical composition, porosity, and internal defects are studied using FTIR, X-ray photoelectron spectroscopy (XPS), Electron energy loss spectroscopy (EELS), and ellipsometric porosimetry. It is shown that the films have a silica like skeleton but also contain suboxides related to the presence of Si—C bonds.

The electronic structure and charge transport of periodic mesoporous organosilica low-κ dielectric films obtained by the CSD method were investigated. The low-κ dielectric properties were investigated in the context of comparison with that of the thermal SiO_2 and strongly nonstoichiometric $SiO_{x<2}$. According to the analysis of XPS spectra and a photoluminescence study, the low-κ dielectric films contain oxygen-deficient centers (vacancies). It is proposed that these centers can recombine forming Si—Si bonds. The oxygen vacancy concentration increases after the sample bombardment with Ar$^+$ ions. The bulk plasmon energy for the PMO low-κ dielectric of 21.7 eV is very close to the one for SiO_x with $x \approx 1.2$. The bandgap value of 6.3 ± 0.3 eV for the PMO low-κ dielectric was found. The lower value in comparison with the published ones for the OSG low-κ dielectric is explained by the relatively high defect state density near the PMO low-κ dielectric

valence-band edge. The EELS data confirm the presence of defects in the studied low-κ dielectric film associated with excess silicon by demonstrating the peaks that can be attributed to the Si—Si—Si cluster and Si—Si bonds, as it is valid for SiO_2. According to the data obtained by Raman spectroscopy, the Si—Si bond concentration in the studied film does not exceed a few atomic percents, and there are no silicon clusters.

The current–voltage characteristics of the studied PMO low-κ dielectric films at different temperatures were analyzed using six transport models. It was found that the Frenkel model of thermal ionization of an isolated Coulomb trap in an electric field, the Hill–Adachi model of overlapping adjacent Coulomb traps, the Shklovskii–Efros percolation model of charge movement in a fluctuating potential, and the Makram-Ebeid–Lannoo model of isolated trap multi-phonon ionization describe the charge transport mechanism in the PMO low-κ dielectric only formally, whereas the agreement with the experiment is achieved at non-physical model parameters. Both qualitatively and quantitatively experimental current–voltage characteristics of the PMO low-κ dielectric are described by the Nasyrov–Gritsenko PATT model of phonon-assisted electron tunneling between traps. The best agreement of calculations and experiments over the entire field range is achieved by using this model considering the space charge through the Poisson equation and charge carrier kinetics through the SRH equations. The electron effective mass in the studied film is 0.42 m_e, and the trap concentration is 3×10^{21} cm^{-3}. The thermal and optical trap energies in the studied films are 1.6 eV and 3.2 eV. The traps with the specified trap energies in SiO_2 are Si—Si bonds. Thus, it can be concluded that the charge transport through the PMO low-κ dielectric is described by the phonon-assisted electron tunneling between the neighboring traps, and these traps are Si—Si bonds.

SUPPLEMENTARY MATERIAL

See the supplementary material for FTIR spectra showing presence of —CH_2—CH_2— bridging groups in the studied organosilicate glass.

ACKNOWLEDGMENTS

REFERENCES

[1]M. R. Baklanov, P. S. Ho, and E. Zschech, *Advanced Interconnects for ULSI Devices* (Wiley, 2012).

[2]R. H. Havemann and J. A. Hutchby, Proc. IEEE **89**, 586 (2001).

[3]S. Z. Yu, T. K. S. Wong, K. Pita, and X. Hu, J. Vac. Sci. Technol. B **20**, 2036 (2002).

[4]Y. H. Xu, Y. P. Tsai, K. N. Tu, B. Zhao, Q. Z. Liu, M. Brongo, G. T. T. Sheng, and C. H. Tung, Appl. Phys. Lett. **75**, 853 (1999).

[5]W. Volksen, R. D. Miller, and G. Dubois, Chem. Rev. **110**, 56 (2010).

[6]M. R. Baklanov, K. Maex, and M. Green, *Dielectric Films for Advanced Microelectronics* (Wiley, Chichester, 2007).

[7]D. J. Michalak, J. M. Blackwell, J. M. Torres, A. Sengupta, L. E. Kreno, J. S. Clarke, and D. Pantuso, J. Mater. Res. **30**, 3363 (2015).

[8]K. Lionti, W. Volksen, T. Magbitang, M. Darnon, and G. Dubois, ECS J. Solid State Sci. Technol. **4**, N3071 (2015).

[9]L. Zhang, J. F. de Marneffe, N. Heylen, G. Murdoch, Z. Tokei, J. Boemmels, S. De Gendt, and M. R. Baklanov, Appl. Phys. Lett. **107**, 092901 (2015).

[10]R. Nenashev, Y. J. Wang, C. H. Liu, N. Kotova, K. Vorotilov, J. Zhang, S. H. Wei, D. Seregin, A. Vishnevskiy, J. Leu, and M. R. Baklanov, ESC J. Solid State Sci. Technol. **6**, N182 (2017).

[11]G. Dubois, W. Volksen, T. Magbitang, R. D. Miller, D. M. Gage, and R. H. Dauskardt, Adv. Mater. **19**, 3989 (2007).

[12]G. Dubois, W. Volksen, T. Magbitang, M. H. Sherwood, R. D. Miller, D. M. Gage, and R. H. Dauskardt, J. Sol-Gel Sci. Technol. **48**, 187 (2008).

[13]E. N. Ogawa and O. Aubel, "Electrical breakdown in advanced interconnect dielectrics," in *Advanced Interconnects for ULSI Devices*, edited by M. R. Baklanov, P. S. Ho, and E. Zschech (Wiley, 2012), pp. 369–434.

[14]B. Jinnai, T. Nozawa, and S. Samukawa, J. Vac. Sci. Technol. B **26**, 1926 (2008).

[15]Z. Tokei, J. Van Aelst, C. Waldfried, O. Escorcia, P. Roussell, O. Richard, Y. Travaly, G. P. Beyer, and K. Maex, IEEE Inter. Reliab. Phys. Sympos. Proc. **43**, 495 (2005).

[16]M. Krishtab, J. F. De Marneffe, S. Armini, J. Meersschaut, H. Benders, C. Wilson, and S. De Gendt, Appl. Surf. Sci. **485**, 170 (2019).

[17]M. R. Baklanov, L. Zhao, E. Van Besien, and M. Pantouvaki, Microelectron. Eng. **88**, 990 (2011).

[18]C. Wu, Y. Li, M. R. Baklanov, and K. Croes, ECS J. Solid State Sci. Technol. **4**, N3065 (2015).

[19]T. Breuer, U. Kerst, C. Boit, E. Langer, H. Ruelke, and A. Fissel, J. Appl. Phys. **112**, 124103 (2012).

[20]K. A. Nasyrov, V. A. Gritsenko, Y. N. Novikov, E. H. Lee, S. Y. Yoon, and C. W. Kim, J. Appl. Phys. **96**, 4293 (2004).

[21]Y. N. Novikov, V. A. Gritsenko, and K. A. Nasyrov, Appl. Phys. Lett. **94**, 222904 (2009).

[22]D. R. Islamov, V. A. Gritsenko, T. V. Perevalov, O. M. Orlov, and G. Y. Krasnikov, Appl. Phys. Lett. **109**, 052901 (2016).

[23]V. A. Gritsenko, T. V. Perevalov, and D. R. Islamov, Phys. Rep. **613**, 1 (2016).

[24]V. A. Gritsenko, T. V. Perevalov, V. A. Voronkovskii, A. A. Gismatulin, V. N. Kruchinin, V. S. Aliev, V. A. Pustovarov, I. P. Prosvirin, and Y. Roizin, ACS Appl. Mater. Inter. **10**, 3769 (2018).

[25]M. S. Lebedev, V. N. Kruchinin, M. Y. Afonin, I. V. Korolkov, A. A. Saraev, A. A. Gismatulin, and V. A. Gritsenko, Appl. Surf. Sci. **478**, 690 (2019).

[26]C. Wu, Y. Li, A. Lesniewska, O. V. Pedreira, J. F. de Marneffe, I. Ciofi, P. Verdonck, M. R. Baklanov, J. Bommels, I. De Wolf, Z. Tokei, and K. Croes, J. Appl. Phys. **118**, 164101 (2015).

[27]Y. F. Lu, R. Ganguli, C. A. Drewien, M. T. Anderson, C. J. Brinker, W. L. Gong, Y. X. Guo, H. Soyez, B. Dunn, M. H. Huang, and J. I. Zink, Nature **389**, 364 (1997).

[28]A. Palov, T. V. Rakhimova, M. B. Krishtab, and M. R. Baklanov, J. Vac. Sci. Technol. B **33**, 020603 (2015).

[29]S. Adachi, *Optical Constants of Crystalline, and Amorphous Semiconductors: Numerical Data, and Graphical Information* (Springer Science & Business Media, New York, 1999).

[30]E. V. Spesivtsev, S. V. Rykhlitskii, V. A. Shvets, Optoelectron. Instrum. Data Process. **47**, 419 (2011).

[31]M. R. Baklanov, K. P. Mogilnikov, V. G. Polovinkin, and F. N. Dultsev, J. Vac. Sci. Technol. B **18**, 1385 (2000).

[32]K. P. Mogilnikov, D. C. Che, M. R. Baklanov, K. N. Xu, and K. D. Xu, in *2017 China Semiconductor Technology International Conference* (*CSTIC 2017*) (IEEE, 2017).

[33]T. V. Perevalov, V. A. Volodin, G. N. Kamaev, G. K. Krivyakin, V. A. Gritsenko, and I. P. Prosvirin, J. Non-Cryst. Solids **529**, 119796 (2020).

[34]B. Garrido, J. Samitier, S. Bota, C. Dominguez, J. Montserrat, and J. R. Morante, J. Non-Cryst. Solids **187**, 101 (1995).

[35]P. Giannozzi, O. Andreussi, T. Brumme, O. Bunau, M. B. Nardelli, M. Calandra, R. Car, C. Cavazzoni, D. Ceresoli, M. Cococcioni, N. Colonna, I. Carnimeo, A. Dal Corso, S. de Gironcoli, P. Delugas, R. A. DiStasio, A. Ferretti, A. Floris, G. Fratesi, G. Fugallo, R. Gebauer, U. Gerstmann, F. Giustino, T. Gorni, J. Jia, M. Kawamura, H. Y. Ko, A. Kokalj, E. Kucukbenli, M. Lazzeri, M. Marsili, N. Marzari, F. Mauri, N. L. Nguyen, H. V. Nguyen, A. Otero-de-la-Roza, L. Paulatto, S. Ponce, D. Rocca, R. Sabatini, B. Santra, M. Schlipf, A. P. Seitsonen, A. Smogunov, I. Timrov, T. Thonhauser, P. Umari, N. Vast, X. Wu, and S. Baroni, J. Phys. Condens. Matter. **29**, 465901 (2017).

[36]T. V. Perevalov, Phys. Solid State **60**, 423 (2018).

[37]A. Grill and D. A. Neumayer, J. Appl. Phys. **94**, 6697 (2003).

[38]M. R. Baklanov, J. F. de Marneffe, D. Shamiryan, A. M. Urbanowicz, H. L. Shi, T. V. Rakhimova, H. Huang, and P. S. Ho, J. Appl. Phys. **113**, 041101 (2013).

[39]K. Vorotilov, V. Petrovsky, and V. Vasiliev, J. Sol-Gel Sci. Technol. **5**, 173 (1995).

[40]P. C. Sukanek, J. Electrochem. Soc. **138**, 1712 (1991).

[41]C. Y. Kim, A. S. Jung, and C. K. Choi, J. Korean Phys. Soc. **53**, 2621 (2008).

[42]J. Heo, H. J. Kim, J. Han, and J. W. Shon, Thin Solid Films **515**, 5035 (2007).

[43]Y. N. Novikov and V. A. Gritsenko, J. Appl. Phys. **110**, 014107 (2011).

[44]N. J. Trujillo, Q. G. Wu, and K. K. Gleason, Adv. Funct. Mater. **20**, 607 (2010).

[45]V. Gritsenko and H. Wong, Crit. Rev. Solid State Mater. Sci. **36**, 129 (2011).

[46]M. J. Jackman, A. G. Thomas, and C. Muryn, J. Phys. Chem. C **119**, 13682 (2015).

[47]G. Pacchioni and G. Ierano, Phys. Rev. Lett. **79**, 753 (1997).

[48]T. Tamura, G. H. Lu, R. Yamamoto, and M. Kohyama, Phys. Rev. B **69**, 195204 (2004).

[49]P. P. Xue, D. F. Pei, H. F. Zheng, W. Y. Li, V. V. Afanas'ev, M. R. Baklanov, J. F. de Marneffe, Y. H. Lin, H. S. Fung, C. C. Chen, Y. Nishi, and J. L. Shohet, Thin Solid Films **616**, 23 (2016).

[50]M. T. Nichols, W. Li, D. Pei, G. A. Antonelli, Q. Lin, S. Banna, Y. Nishi, and J. L. Shohet, J. Appl. Phys. **115**, 094105 (2014).

[51]F. G. Bell and L. Ley, Phys. Rev. B **37**, 8383 (1988).

[52]M. C. Cheynet and T. Epicier, Philos. Mag. **84**, 1753 (2004).

[53]A. Grill, J. Appl. Phys. **93**, 1785 (2003).

[54]H. Zheng, S. W. King, V. Ryan, Y. Nishi, and J. L. Shohet, Appl. Phys. Lett. **104**, 062904 (2014).

[55]X. Guo, H. Zheng, S. W. King, V. V. Afanas'ev, M. R. Baklanov, J. F. de Marneffe, Y. Nishi, and J. L. Shohet, Appl. Phys. Lett. **107**, 082903 (2015).

[56]R. Williams, Phys. Rev. **140**, A569 (1965).

[57]E. Vella, F. Messina, M. Cannas, and R. Boscaino, Phys. Rev. B **83**, 174201 (2011).

[58]Z. A. Weinberg, G. W. Rubloff, and E. Bassous, Phys. Rev. B **19**, 3107 (1979).

[59]R. J. Powell and M. Morad, J. Appl. Phys. **49**, 2499 (1978).

[60]K. Awazu, H. Kawazoe, and K. Muta, J. Appl. Phys. **70**, 69 (1991).

[61]V. S. Kortov, A. F. Zatsepin, S. V. Gorbunov, and A. M. Murzakaev, Phys. Solid State **48**, 1273 (2006).

[62]L. Skuja, J. Non-Cryst. Solids **239**, 16 (1998).

[63]K. Raghavachari, D. Ricci, and G. Pacchioni, J. Chem. Phys. **116**, 825 (2002).

[64]H. Imai, K. Arai, H. Imagawa, H. Hosono, and Y. Abe, Phys. Rev. B **38**, 12772 (1988).

[65]N. Terada, T. Haga, N. Miyata, K. Moriki, M. Fujisawa, M. Morita, T. Ohmi, and T. Hattori, Phys. Rev. B **46**, 2312 (1992).

[66]L. N. Skuja, A. N. Streletsky, and A. B. Pakovich, Solid State Commun. **50**, 1069 (1984).

[67]J. Zhang, Y. Wang, J. Zhang, H. Xu, C. Liu, S. Wei, and M. R. Baklanov, in *Proceedings of Advanced Metallization Conference, Tokyo* (Tokyo Institute of Technology, 2019), pp. 110–111.

[68]M. A. Garcia, S. E. Paje, M. A. Villegas, and J. Llopis, Mater. Lett. **43**, 23 (2000).

[69]V. A. Volodin, V. A. Gritsenko, and A. Chin, Tech. Phys. Lett. **44**, 424 (2018).

[70]V. A. Volodin, G. N. Kamaev, V. A. Gritsenko, A. A. Gismatulin, A. Chin, and M. Vergnat, Appl. Phys. Lett. **114**, 233104 (2019).

[71]J. Frenkel, Phys. Rev. B **54**, 647 (1938).

[72]J. Frenkel, Technol. Phys. USSR **5**, 685 (1938).

[73]R. M. Hill, Philos. Mag. **23**, 59 (1971).

[74]H. Adachi, Y. Shibata, and S. Ono, J. Phys. D: Appl. Phys. **4**, 988 (1971).

[75]B. I. Shklovskii and A. L. Efros, Sov. Phys. Usp. **18**, 845 (1975).

[76]B. I. Shklovskii and A. L. Efros, *Electronic Properties of Doped Semiconductors* (Springer-Verlag, Berlin, 1984).

[77]S. S. Makram-Ebeid and M. Lannoo, Phys. Rev. B **25**, 6406 (1982).

[78]K. A. Nasyrov and V. A. Gritsenko, J. Appl. Phys. **109**, 093705 (2011).

[79]K. A. Nasyrov and V. A. Gritsenko, Phys. USP **56**, 999 (2013).

[80]B. Brar, G. D. Wilk, and A. C. Seabaugh, Appl. Phys. Lett. **69**, 2728 (1996).